Supporting Information for

Highly Active Mixed-Metal Nanosheet Water Oxidation Catalysts Made by Pulsed-Laser Ablation in Liquids

Bryan M, Hunter, James D. Blakemore, Mark Deimund, Harry B. Gray, Jay R. Winkler, and Astrid M. Müller

Beckman Institute and Division of Chemistry and Chemical Engineering, California Institute of Technology, M/C 139-74, Pasadena, California 91125; correspondence should be addressed to astridm@caltech.edu.

1. General Experimental Conditions and Apparatus

Materials and Methods. Nanomaterial synthesis by pulsed laser ablation in liquids was performed in the Beckman Institute Laser Resource Center at California Institute of Technology. X-ray photoelectron spectroscopy was carried out at the Molecular Materials Research Center (Beckman Institute at California Institute of Technology). Transmission electron micrographs were collected at the Beckman Resource Center for Transmission Electron Microscopy (California Institute of Technology).

All chemicals were used as received. Deionized water was obtained from a Barnstead Diamond Nanopure system and had a resistivity of ≥16 MΩ cm^{-1}.

Synthesis. Mixed metal nanomaterials were synthesized using the method of pulsed laser ablation in liquids (PLAL). Suspensions of iron (Alfa, −200 mesh, 99+%) or nickel (Alfa, −150+200 mesh, 99.8%) powders were stirred in 10 mL aqueous metal nitrate solutions using a magnetic stirrer in a 30 mL glass beaker at room temperature in ambient air. For ablation, 0.5 g iron powder or 2.0 g nickel powder were used. With iron as ablation target, the liquid consisted of 10 mL pH 10.0 water (adjusted with potassium hydroxide, Mallinckrodt) with nickel nitrate ($Ni(NO_3)_2 \cdot 6H_2O$, Alfa, 98%) concentrations of 0.1 M, 1.0 M, and 3.0 M. With nickel as ablation target, the liquid was 10 mL water with iron nitrate ($Fe(NO_3)_3 \cdot 9H_2O$, Alfa, 98.0–101.0%) concentrations of 0.01 M and 0.1 M. Nanomaterials with more than two metals were made from 0.5 g iron powder suspended in 10 mL of a solution of 3.0 M nickel nitrate and 0.015 M titanium(IV) oxide bis(acetylacetonate) (Strem, >95%) in 10 mL pH 10.0 water (adjusted with KOH). Some solutions also contained 0.023 M lanthanum nitrate ($La(NO_3)_3 \cdot 6H_2O$, Sigma-Aldrich, ≥99%). Beakers and stir bars were thoroughly cleaned with *aqua regia* before use.

A 355 nm, 8 ns pulse laser beam, provided by the third harmonic of a 10 Hz Q-switched Nd:YAG laser (Spectra-Physics Quanta-Ray PRO-Series), was focused 0.5 mm below the surface of the liquid with a 100 mm focal length plano-convex quartz lens. Each sample was irradiated for 60 min. Laser pulse energies were either 90 or 210 mJ/pulse.

After synthesis, nanoparticle suspensions were separated from the metallic ablation targets using a strong magnet. Solid nanoparticulate powders were obtained by centrifugation and washing with water until the supernatant did not show any metal nitrate absorption. The nanoparticles were then washed twice with acetone (EMD, OmniSolv®) and dried under vacuum. A high precision balance (Sartorius CPA225D) was used to weigh the nanoparticle powders. Around 5 mg material were suspended in water to make 2 mg mL^{-1} suspensions; 20 μL of these were drop cast on freshly-cleaved highly-ordered pyrolytic graphite (HOPG) working electrodes and dried in ambient air under a heat lamp at 50°C, resulting in a catalyst loading of 40 μg.

Electrodeposited nickel oxide catalyst was prepared according to the procedure published by Nocera.[1] In detail, we dissolved 2.18 g $Ni(NO_3)_2 \cdot 6H_2O$ in 5 mL water and added this solution to 75 mL rapidly stirred 0.1 M pH 9.20 aqueous sodium borate buffer, which immediately became turbid. The sodium borate buffer was made from sodium tetraborate ($Na_2B_4O_7 \cdot 10H_2O$, Baker, 101.4%) and its pH was adjusted by adding boric acid (H_3BO_3, Mallinckrodt, 99.9%). The filtrate of the suspension was used as the electrolyte; the working electrode was a freshly cleaved HOPG electrode. An Ag/AgCl/3.0 M NaCl reference electrode

(Bioanalytical Systems, Inc.; measured to be +0.212 V vs NHE, reference electrode calibration was described previously)[2] and a Ni gauze (Alfa) counter electrode were used. We passed 51 mC charge with an applied voltage of 1.312 V vs. NHE; faradaically, we deposited 530 nmol Ni, which corresponds to 40 μg NiO. Before catalytic activity testing the electrodeposited films were thoroughly washed with water.

Physical Characterization. X-ray photoelectron spectra (XPS) were taken using a Surface Science Instruments M-probe surface spectrometer. Monochromatic Al Kα radiation (1486.6 eV) was used to excite electrons from the samples, which had been drop-cast on clean Cu foil and dried in ambient air at room temperature. The sample chamber was maintained at $<5\times10^{-9}$ Torr. Survey scans from 0 to 1000 eV were carried out to identify the elements present in the nanoparticles. Binding energies were referenced to the C 1s peak arising from adventitious carbon, taken to have a binding energy of 284.8 eV.[3] High-resolution spectra were collected for the Fe 2p, Ni 2p, Ti 2p, La 3d, N 1s, and O 1s regions. Quantitative peak areas were derived after Shirley background subtraction[4] and using relative sensitivity factors. Binding energies were obtained from the same peak fits. Quantitative XPS analysis was performed with CasaXPS (Version 2.3.16 PR 1.6).

X-ray diffraction (XRD) data were collected with a Bruker D2 PHASER diffractometer. Monochromatic Cu Kα radiation (1.5418 Å; tube power 30 kV, 10 mA) was used; the instrument was equipped with 0.1° divergence, 1.5° Soller, and 0.6 mm detector slits, and had a 3-mm secondary anti-scatter screen. Diffracted radiation was collected with a Lynxeye detector. The instrument resolution was 0.05° in 2θ, and the counting time was 3 seconds per step, resulting in a total scan time of about 75 min for each sample. Solid samples were deposited with vaseline (X-Alliance GmbH) on a zero-diffraction silicon plate (MTI Corporation). XRD background subtraction, Scherrer and pattern analysis were performed with the Bruker DIFFRAC.SUITE software coupled to the International Centre for Diffraction Data powder diffraction file database (ICDD, PDF-2 Release 2012).

Raman spectra of neat solid catalysts were collected at room temperature in ambient air with a Renishaw M1000 micro-Raman spectrometer. A 50× magnification objective and a 50-μm slit, resulting in 4 cm^{-1} resolution, were used. The laser excitation wavelength was 514.3 nm (Cobolt Fandango™ 100 laser), the power at the sample was 213 μW (1% laser power, measured with a Thorlabs PM100USB power meter), and depolarized scattered light was detected. The excitation intensity was chosen as to prevent radiation damage of the nanoparticulate powders; collected spectra did not change during repeated scans. The radiation damage threshold was approximated to be at a laser intensity that was three times higher than that applied. Application of 10% laser power through a 50× magnification objective led to immediate radiation damage, and a dark spot was visible on the sample when viewed through the microscope. Focusing the 10% power laser beam through a 20× magnification objective led to gradual sample degradation over multiple scans, which was also observed by visual inspection with the microscope. The instrument's autofocus function was used to maximize the signal-to-noise ratio. The accumulation time was 10 s, and 8 scans were averaged for each sample. The measured Raman shifts were calibrated against a Si standard. Spectra were compared to reference spectra from the RRUFF database, which were collected with 532 nm excitation and depolarized detection.[5]

Attenuated total reflectance infrared spectra of neat nanoparticulate powders were collected with a Thermo Nicolet iS50 FT-IR spectrometer, equipped with a Pike Technologies GladiATR

accessory plate and an uncooled pyroelectric deuterated triglycine sulfate (DTGS) detector. In the 50 to 700 cm^{-1} range, a far-infrared multilayer beamsplitter was used and a measured water vapor spectrum was subtracted from the data; in the 400 to 4000 cm^{-1} range, a KBr beamsplitter was used. Spectra of the solid nanoparticulate powders were collected at room temperature in ambient air, and 132 scans were averaged for each sample.

Transmission electron microscopy (TEM) measurements were performed with an FEI Tecnai T-12. For each material, 2 μL of a suspension of 2 mg mL^{-1} nanoparticles in water were drop cast on a 200 mesh Cu grid coated with Formvar carbon (Ted Pella), which was placed on a Kimwipe. The nanoparticles were dispersed on the hydrophobic grid surface by adding 10 μL isopropanol. The average diameter of the nanoparticles was determined using the ImageJ software.[6]

Specific surface areas were determined by Brunauer-Emmett-Teller (BET) measurements, using a Quantachrome Autosorb iQ instrument. Adventitious adsorbates were removed under vacuum by heating approximately 40 mg of each catalyst powder at a rate of 10 K min^{-1} from room temperature to 423 K, holding it there for 1 hour, followed by heating to 573 K at a rate of 10 K min^{-1}, where it remained for 6 hours, and subsequent cooling to room temperature. Virtually identical sizes of catalysts before and after heating for BET analysis were found by TEM imaging. Multipoint argon adsorption-desorption isotherms were collected at 87.45 K, and the specific surface areas were calculated with the instrument's built-in software, based on the BET equation.

Electrochemical Characterization. Cyclic voltammetry, Tafel, and chronoamperometry data were collected at room temperature. For all electrochemical measurements, the electrolyte was aqueous 1.0 M pH 14.0 KOH (Mallinckrodt); an Hg/HgO reference electrode (CH Instruments), a Ni gauze (Alfa) counter electrode, and HOPG working electrodes with 40 μg catalyst on them were used. Working electrodes for cyclic voltammetry, faradaic oxygen yield, and chronoamperometry data consisted of upward-facing HOPG (GraphiteStore, surface area: 0.09 cm^2) electrodes. Their preparation is described elsewhere;[2] the only difference was that the glass tubes were u-shaped at one end to make the HOPG electrode surface face upwards, which facilitated measurements with extensive oxygen evolution because it allowed the generated gas to bubble up. Working electrodes were cleaned by sonication for 10 min in concentrated hydrochloric acid, washed with water, and their surfaces were polished using 400 and 600 grit sandpaper, after which the graphite was cleaved with adhesive tape to obtain a fresh HOPG surface for each catalyst.

Cyclic voltammograms were measured at 10 mV s^{-1} scan rate with a Gamry Reference 600 potentiostat. Tafel data were recorded using a rotating disk electrode (RDE) apparatus. Measurements were carried out in a 100 mL three-neck round-bottom flask with a Pine MSR variable speed rotator used at 1,500 rpm and a Princeton Applied Research Parstat 4000 potentiostat. The dwell time at each applied potential point was 5 min to reach steady-state conditions. The disk electrode was made of HOPG with stabilizing epoxy around its side (surface area: 0.13 cm^2). The current density *versus* potential data were post-measurement corrected for uncompensated resistance losses (see below). All potentials reported here are relative to the normal hydrogen electrode (NHE), and current densities are per geometric area.

The ohmic drop (uncompensated resistance, R_u) was experimentally determined for an HOPG working electrode, either blank or with 40 μg nanoparticulate catalyst loading, using a

Gamry Reference 600 potentiostat and its built-in "measure R_u" utility that uses the current interrupt method. The working electrode was swept between 0.107 and 0.907 V vs. NHE and R_u values were collected. The averages of 3 R_u values were plotted as a function of applied potential, and the data were fit with a line (Figure S1).

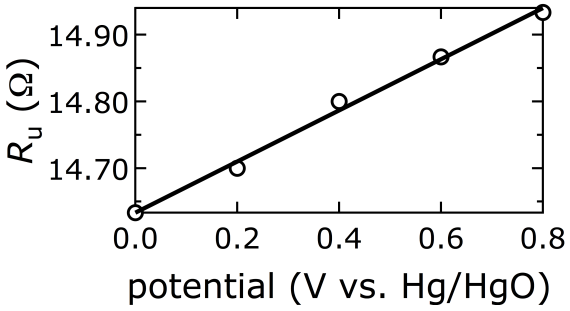

Figure S1: Determination of R_u for post-measurement iR drop correction; circles, measured data; line, linear fit.

Post-measurement iR drop correction was performed according to Oelßner.[7] We chose to use this method, where we experimentally determined R_u for our nanoparticulate catalysts under the same conditions as all other electrochemical measurements, because automatic iR-correction is inherently problematic for high-surface-area materials. In detail, the true polarization potential E_p was calculated from the applied potential E_a, the measured current i, and the uncompensated resistance R_u as $E_p = E_a - iR_u$.

Faradaic yields of oxygen evolution data were collected with an apparatus described previously.[2] A glass cell was filled with 65 mL electrolyte, leaving 59 mL headspace, in which the O_2 concentration was measured. A potential of 0.857 V vs. NHE was applied for 30 min, using a Gamry 600 potentiostat. The electrolysis chamber was water-jacketed and kept at a constant temperature of (22.0±0.5)°C to ensure a stable response from the O_2 sensor. In a typical experiment, based on the charge transferred, we expected 284 μL of O_2 evolved and detected 297 μL. This confirmed essentially 100 % oxygen evolution within the error (10%) of our method.

Long-term stability measurements were performed using a Gamry 600 potentiostat and a working electrode, onto which 40 μg catalyst had been drop cast from a 2 mg mL^{-1} suspension that also contained 80 μg mL^{-1} Nafion 117 (Aldrich). Nafion was added for chronoamperometry experiments to improve the mechanical stability of catalyst films on HOPG during oxygen evolution. A potential of 0.654 V vs. NHE was applied for 5.5 hours and the current was recorded.

Data analysis and graphing was performed with Igor Pro 6.34 (Wavemetrics).

2. Physical Characterization

2.1. X-Ray Photoelectron Spectra

XPS data were collected to identify nanoparticle compositions by peak integrations of high-resolution spectra of the Fe 2p, Ni 2p, O 1s, N 1s, Ti 2p, and La 3d regions, where applicable. The regions were chosen as to collect data on transitions with the highest x-ray ionization cross-sections.[8] Since the x-ray ionization cross-section of Ti 2p is a factor of 5.4 lower that that of

La 3d,[8] and 1.5 times less Ti^{4+} than La^{3+} was added to the ablation liquid, no Ti photoelectrons were detected. We deliberately did not attempt to quantify oxygen content from XPS data because the amount of this element is regularly overestimated; oxygen also occurs in other sources, such as adventitious carbon species and oxides of the underlying copper substrate.

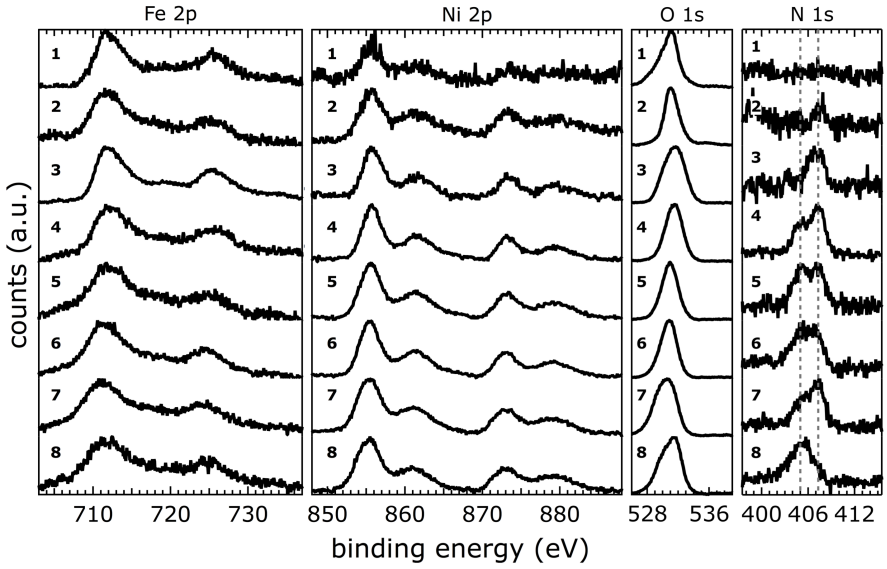

Figure S2: XPS data of catalysts **1** to **8** in the Fe 2p, Ni 2p, O 1s, and N 1s regions. The gray dashed lines are at the N 1s binding energies at 405.1 and 407.3 eV.

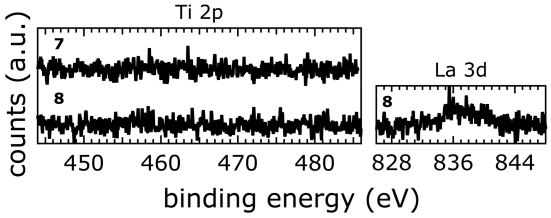

Figure S3: XPS data of catalysts **7** and **8** in the Ti 2p and La 3d regions.

The Fe 2p core level spectra of catalysts **1** to **8** showed peaks consistent with iron oxides and oxyhydroxides,[9] with Fe $2p_{3/2}$ binding energies close to 710.9 eV. It is not possible to distinguish the different Fe phases in our materials from Fe 2p XPS data, as various iron oxides and oxyhydroxides, such as FeO, Fe_2O_3, Fe_3O_4, and Fe(O)OH, have similar Fe core-level binding energies and spectral shapes.[9] The Ni 2p core-level binding energies of catalysts **1** to **8** were indicative of $Ni(OH)_2$ or Ni(O)OH,[10,11] with Ni $2p_{3/2}$ binding energies close to 855.7 eV. The O 1s spectra of **1** to **8** exhibited, among contributions from adventitious oxygen species, two peaks centered around 528.8 eV and 531.4 eV, as expected for Fe or Ni oxide and hydroxide species, respectively.[10] The N 1s core level spectra of catalysts **1** to **8** showed two peaks with binding energies at 407.3 eV and 405.1 eV.

2.2. X-Ray Diffraction Data

XRD data were collected to determine crystalline phases and crystallite sizes by Scherrer analysis. Note that peak widths were determined by factoring in multiple diffraction lines from the corresponding PDF, where applicable. Overlapping diffraction lines may give rise to peaks that appear broader in the total intensity spectra. As a result, peak broadness in the total intensity spectrum does not necessarily correlate to the actual crystalline domain size. The XRD data were fit by the automatic search/match function of the Bruker software DIFFRAC.SUITE, using a database based on macroscopic crystals. Peak positions were in agreement with known XRD patterns as follows. The Fe-rich catalysts were amorphous, **1** and **3** completely so, and **2** predominantly so, with some broad peaks that were assigned to poorly crystallized Fe_3O_4 (powder diffraction file no. 00-019-0629) and γ-Fe_2O_3 (PDF 00-039-1346). XRD data of the more Ni-rich catalysts **4** to **8** showed mainly the crystalline layered double hydroxide (LDH) $[Ni_{1-x}Fe_x(OH)_2](NO_3)_y(OH)_{x-y}\bullet nH_2O$ (PDF 00-038-0715, α-(Fe,Ni)$(OH)_2$) and a minor contribution from crystalline Fe(O)OH (PDF 00-029-0713). We could not observe any β-$Ni(OH)_2$ (PDF 00-014-0117) in our catalysts. Catalyst **6** additionally contained crystalline $NiFe_2O_4$ (PDF 01-076-6119). In **7** and **8**, minerals containing added elements were also present; TiO_2 (PDF 01-082-1123) and Fe_2TiO_4 (PDF 00-034-0177) were detected in **7**, whereas crystalline Ni_3TiO_5 (PDF 00-030-0865) and La(Ni,Fe)O_3 (PDF 01-088-0637) were found in **8**.

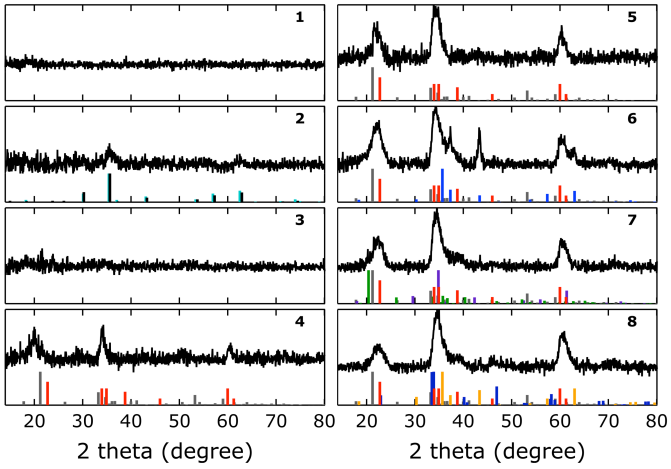

Figure S4: XRD data of catalysts **1** to **8**. Normalized fixed slit intensities of known macroscopic crystals are displayed as vertical lines: black, γ-Fe_2O_3; cyan, Fe_3O_4; red, α-(Fe,Ni)$(OH)_2$; gray, Fe(O)OH; blue, $NiFe_2O_4$; green, TiO_2; purple, Fe_2TiO_4; yellow, Ni_3TiO_5; dark blue, La(Ni,Fe)O_3.

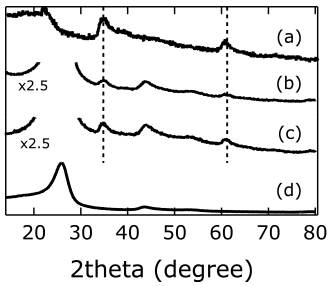

Figure S5: XRD data of catalyst **5** after anodization, (a) on Si, (b) on carbon cloth after 30 min anodization in 1.0 M pH 14.0 aqueous KOH at 0.807 V vs NHE, (c) on carbon cloth before anodization; bare carbon cloth (d).

2.3. Transmission Electron Micrographs

TEM images were taken to obtain nanoparticle sizes. Our intention was to avoid blocking catalytically active surface sites; therefore our nanoparticles were synthesized by PLAL without any surfactants. They naturally aggregated in aqueous suspensions. We prepared very dilute samples on TEM grids, resulting in only a few (aggregated) nanoparticles being imaged per frame. Note that frame-filling nanoparticle patterns will only form by self-assembly of surfactant-capped nanoparticles due to repulsive or attractive forces between surfactant molecules.[12]

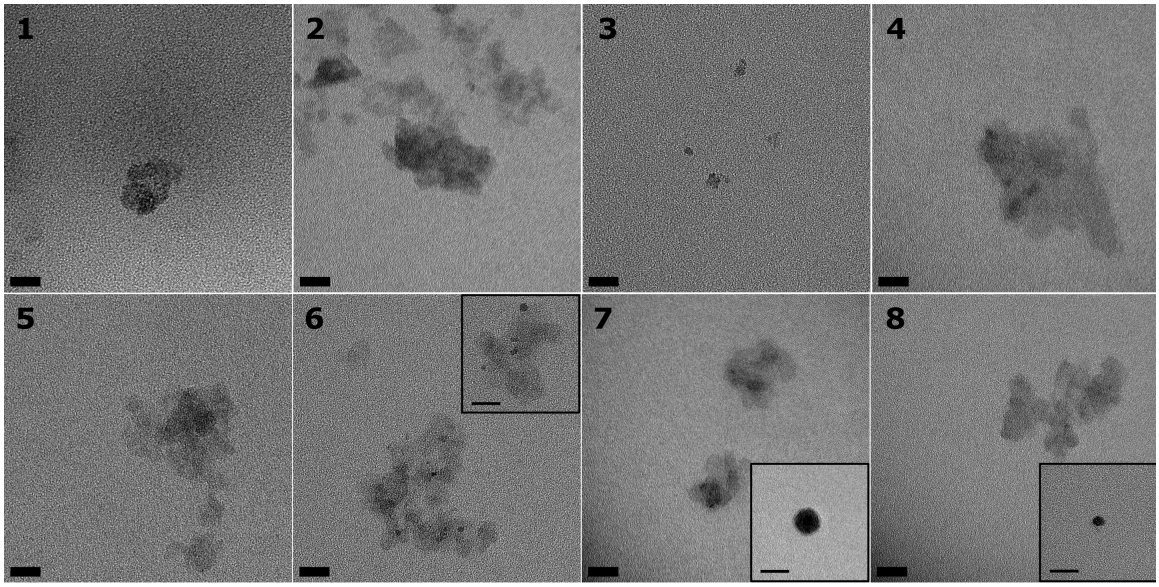

Figure S6: TEM images of water oxidation catalysts **1** to **8**. The insets show particles that imaged with a higher contrast. All scale bars are 20 nm.

Nanocatalyst compositions and sizes are summarized in Table S1. Compositions were derived from XPS peak area quantification. Scherrer analysis of XRD data for catalysts **4** to **8** was used to obtain crystalline domain sizes (materials **1** to **3** were poorly crystallized); the corresponding crystalline phases are given in parentheses. Nanoparticle sizes were determined by TEM image analysis.

Analysis of TEM and XRD data of **6** suggested that smaller, (6.5 ± 0.8) nm particles could be attributed to $NiFe_2O_4$, and larger (13 ± 1) nm nanosheets could be assigned to the layered double hydroxide $[Ni_{1-x}Fe_x(OH)_2](NO_3)_y(OH)_{x-y}\bullet nH_2O$. It became evident from inspection of TEM images of **6** that the smaller ($NiFe_2O_4$) nanoparticles exhibited more contrast, consistent with more spherical shape, than the larger $[Ni_{1-x}Fe_x(OH)_2](NO_3)_y(OH)_{x-y}\bullet nH_2O$ sheets. The spinel $NiFe_2O_4$ crystallizes in the cubic system,[13] rendering the formation of nanoparticles with radial symmetry likely. The double hydroxide $[Ni_{1-x}Fe_x(OH)_2](NO_3)_y(OH)_{x-y}\bullet nH_2O$, however, crystallizes as a layered structure,[14] leading to axially elongated nanosheets. Likewise, differences in TEM contrast, shape, and size were found for catalysts **7** and **8**.

Table S1: Catalyst metal contents, concentrations of both nitrogen species with respect to total metal content, crystalline domain sizes, and nanoparticle sizes.

Catalyst	% Metal			% Nitrogen (405.1 eV binding energy)	% Nitrogen (407.3 eV binding energy)	Crystalline Domain Size (nm)	Nanoparticle Size (nm)
	Fe	Ni	La				
1	95	5	–	0	0	–	22 ± 3
2	86	14	–	0	8	–	10 ± 2
3	70	30	–	1	6	–	7.7 ± 2
4	36	64	–	6	10	12 ± 3 (LDH)	14 ± 2
5	22	78	–	5	5	9 ± 2 (LDH)	12 ± 2
6	30	70	–	5	5	13 ± 3 (LDH) 6.1 ± 0.5 (spinel)	13 ± 2 6.5 ± 0.8
7	23	77	–	3	5	12 ± 3 (LDH)	13 ± 2 19 ± 2
8	29	70	1	8	4	14 ± 4 (LDH)	14 ± 2 8.7 ± 1

2.4. Brunauer-Emmett-Teller Data

BET data were collected to obtain surface areas of the more active water oxidation catalysts **5** to **8**.

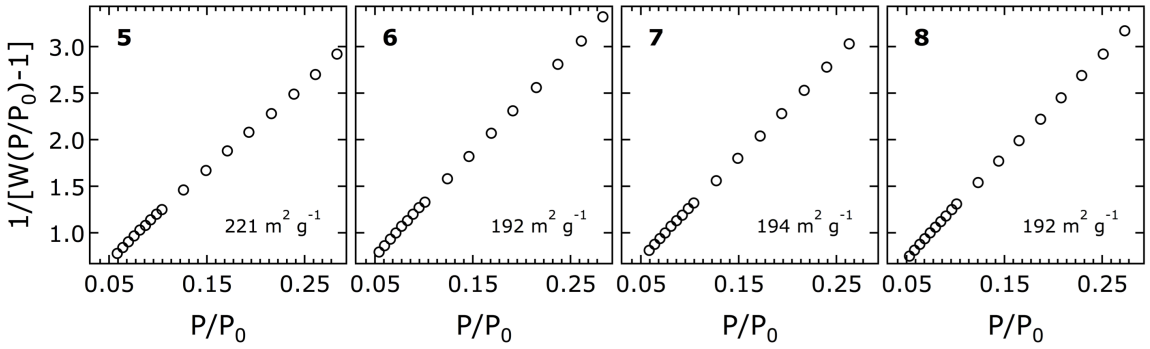

Figure S7: BET data of catalysts **5** to **8**; P/P_0 denotes the relative pressure, and W is the weight of the adsorbed argon.

2.5. Raman Spectra

The Raman spectra of **1** to **3** showed a broad feature centered at around 650 cm^{-1}. In this region, Raman shifts of ferrous-ferric oxides, such as magnetite[15] or ferrihydrite,[16] occur. The broadness observed for **1** to **3**, however, strongly suggests the presence of structurally ill-defined, poorly crystalized materials. The Raman spectra of **4** to **8** were compared to a reference spectrum of mineralogical α-$(Fe,Ni)(OH)_2$[5] and showed good agreement. The strong peaks in the spectra of **4** to **8** at ~1050 cm^{-1} were assigned to inter-layer nitrate ions, consistent with peaks that have previously been observed in electrochemically deposited α-$Ni(OH)_2$ thin films.[17] MacDougall reported that only α-$Ni(OH)_2$ contained measurable nitrate, as formation of crystalline β-$Ni(OH)_2$ occurred with the concurrent loss of interstitial layering; the β-polymorph did not accommodate interstitial ions because of tighter crystal packing.[17]

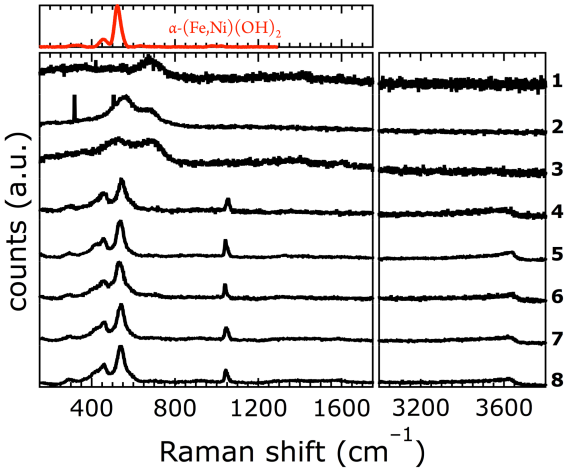

Figure S8: Raman spectra of catalysts **1** to **8** (black). The sharp spikes in the spectrum of **2** are from cosmic ray events. Also depicted is a reference spectrum of mineralogical α-(Fe,Ni)$(OH)_2$ (red, RRUFF ID R070619, collected with 532 nm excitation).[5]

Which $Ni(OH)_2$ phase is catalytically most active is still subject of intense debate. During water oxidation, α-$Ni(OH)_2$ is oxidized to γ-Ni(O)OH, whereas β-$Ni(OH)_2$ is transformed into β-Ni(O)OH; both oxyhydroxides are reduced back to their starting hydroxides during electrochemical cycling.[18-20] It has been a long-held view that β-$Ni(OH)_2$ is more active for oxygen evolution. Studies of electrodeposited amorphous α-$Ni(OH)_2$ and its ageing to β-$Ni(OH)_2$ in basic electrolytes suggested that oxygen evolution occurred at lower onset potential for β-$Ni(OH)_2$/β-Ni(O)OH.[18,21-28] Yachandra and Nocera challenged this notion by correlating structure to activity in a nickel-borate oxygen evolution catalyst.[29] Dai established that crystalline Fe-doped α-$Ni(OH)_2$ on carbon nanotubes is more active than the equivalent β-phase material.[30] And Yan recently synthesized phase-controlled crystalline α- and β-$Ni(OH)_2$ materials and found that the α-polymorph was more active for water oxidation.[31] Our results support the recent findings that α-$Ni(OH)_2$ is highly active for water oxidation.

2.6. Infrared Spectra

Infrared (IR) spectra were collected to shed more light on the compositions of catalysts **5** and **6**. The IR spectra of **5** and **6** showed broad peaks with maxima at 340, 500, and 640 cm^{-1}. The δ(OH) band at 640 cm^{-1} is very sensitive to the amount of water intercalated between the α-$Ni(OH)_2$ layers. Bands, attributed to OH-bending motions, typically appear at ~650 cm^{-1} for $Ni(OH)_2$ with high water content and thus indicate the presence of the α-polymorph. In contrast, for the β-polymorph, the band is shifted to ~520 cm^{-1}. Additionally, the α-polymorph shows broad absorption in the ν(OH) region (3400–3600 cm^{-1}), whereas the β-polymorph features a sharp band at 3640 cm^{-1}.[32] The location and broadness of the δ(OH) and ν(OH) bands in our catalysts **5** and **6** led us to conclude that $[Ni_{1-x}Fe_x(OH)_2](NO_3)_y(OH)_{x-y}\bullet nH_2O$ was the predominant material. The band at 1340 cm^{-1} was further evidence of interstitial nitrates.[33]

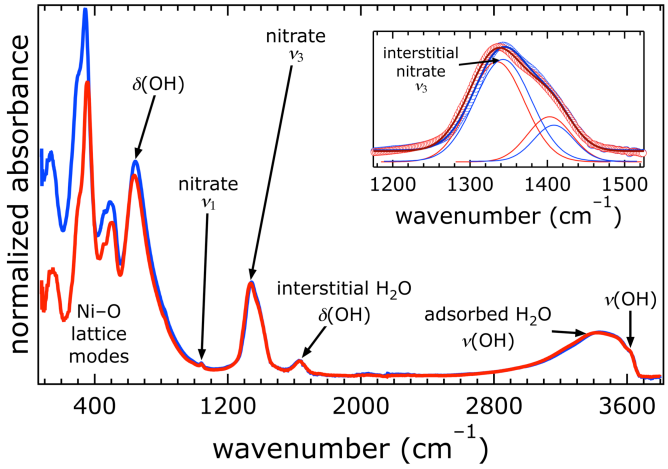

Figure S9: Infrared spectra of catalysts **5** (red) and **6** (blue) with band assignments. The inset shows a magnification of the nitrate (ν_3) region: open circles, data; thick lines, overall fits; thin lines Gaussian peak fits. The band was best fit by two Gaussian distributions, indicating the presence of two distinct species.

The spectrum of $Ni(OH)_2$ with iron incorporation was qualitatively determined from published transmission-mode IR spectra.[22,33] Two materials were used in this analysis, (1) almost exclusively $Ni(OH)_2$ and (2) one of mixed (Ni,Fe) composition, due to aging in KOH for 72 hours. The compositions of these materials were determined by XRD and Mössbauer spectroscopy in the original study.[33]

The IR spectra were digitized from an electronic (PDF) copy of the original manuscript using UN-SCAN-IT v.5.2 software. Transmission values (digitized y-values) were aligned with the wavelength (digitized x-values) for both spectra, omitting points where digitization was not complete for both.

The spectrum of (2) was shifted down vertically by assuming that the common feature at 495 nm is isosbestic in transmission. The spectrum of (1) was scaled by a factor consistent with a second isosbestic point at 670 nm. The absorbance spectra of the two samples was then calculated using $A(x) = 2 - \log[T(x)]$, where $A(x)$ is the absorbance and $T(x)$ is the decimal transmission at the wavelength x.

Finally, the spectrum of mixed (Ni,Fe) 'oxyhydroxide' was approximated by subtracting the absorbance spectrum of (1) from (2). It is plotted as a red dotted line in Figure S10, alongside the normalized absorbance spectrum of (1), graphed as a blue dotted line.

It is important to note that, in the absence of an absolute transmission value, these spectra are only qualitative. They do, however, clearly indicate the direction that the peaks shift upon incorporation of iron into the nickel phase. The growth of features at ~400 cm^{-1} and ~600 cm^{-1} relative to the features at ~350 cm^{-1} and ~650 cm^{-1} is indicative of iron incorporation into the nickel phase. This trend has been observed previously.[34-36]

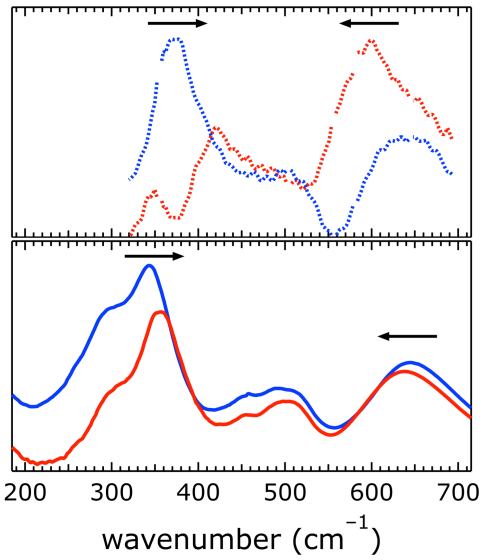

Figure S10: Infrared spectra (solid lines) of catalysts **5** (red) and **6** (blue) with spectral deconvolutions (dotted lines).

3. Electrochemical Characterization

Electrochemical activity of the nanoparticulate catalysts was assessed by cyclic voltammetry and Tafel data, long-term stability was measured by chronoamperometry.

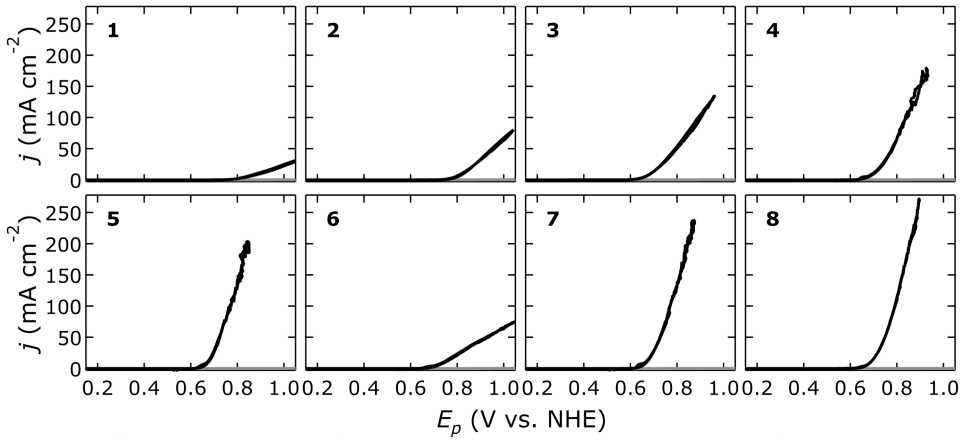

Figure S11: Cyclic voltammograms of catalysts **1** to **8**; *j*, current density, E_p, polarization potential. The disjointed segments in the measured data occurred due to bubble release from the electrode surface.

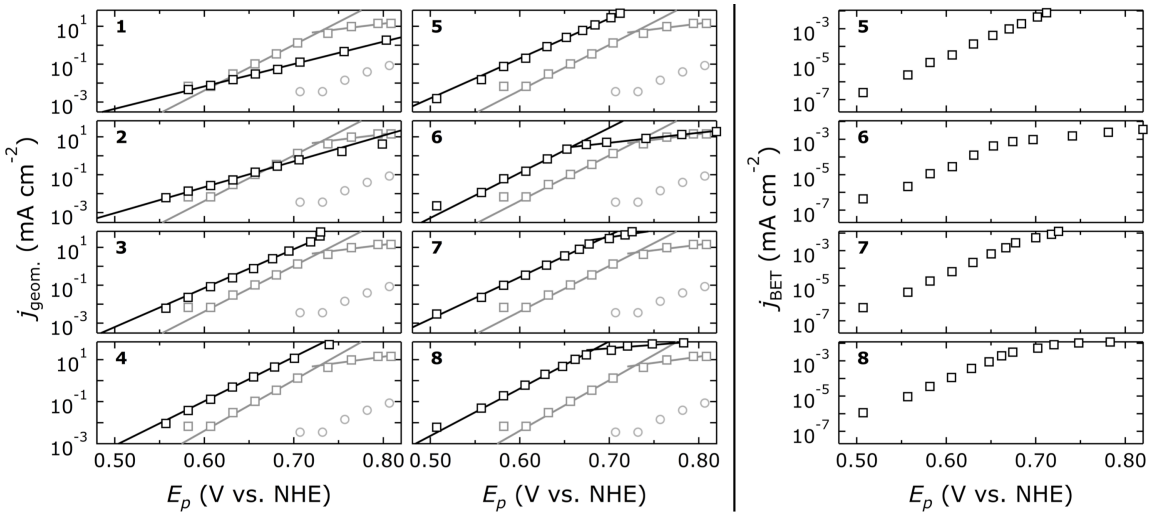

Figure S12: Tafel data of catalysts **1** to **8** (black squares); *j*, current density, E_p, polarization potential. For comparison, Tafel data of electrodeposited nickel oxide (gray squares, same mass loading as catalysts) and bare HOPG (gray circles) are also plotted. The solid lines are fits. Left, current data of **1** to **8** normalized to geometric electrode areas; right, current data of **5** to **8** normalized to BET surface areas.

Plotting the overpotential at 10 mA cm^{-2} vs. the Ni content in the catalyst (from XPS data) shows that the highest water oxidation activity was obtained with the highest Ni content (78%) in the material.

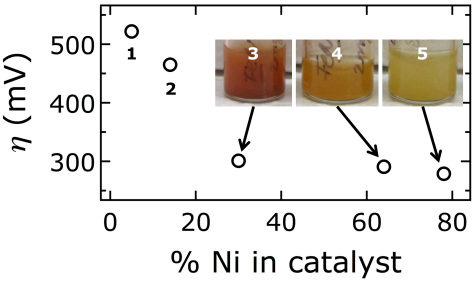

Figure S13: Overpotential η for water oxidation at 10 mA cm^{-2} vs. Ni content for catalysts **1** to **5**. Depicted in the photos are catalysts **3** to **5** in aqueous suspension to visualize their different colors.

Chronoamperometry data showed that catalytic activity of catalysts **5**, **6** and **8** was maintained for more than 5 hours. The current fluctuations were due to formation and release of oxygen bubbles from the electrode surface.

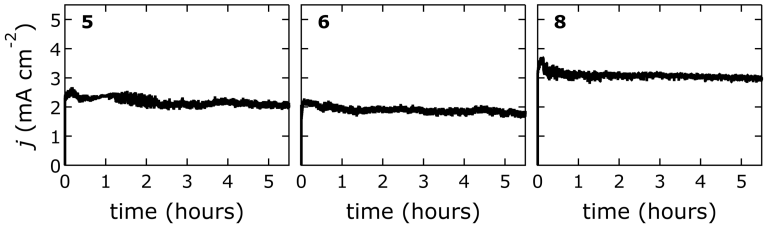

Figure S14: Current density *j* as a function of time data of catalysts **5, 6** and **8**, the applied potential was 0.654 V vs. NHE.

A summary of catalytic activity data is provided in Table S2.

Table S2: Overpotentials η at current densities of 0.5 and 10 mA cm^{-2}, Tafel slopes A, and turnover frequencies (TOF) per gram catalyst at 250 mV and 300 mV overpotential of catalysts **1** to **8** and electrodeposited Ni oxide for comparison.

Catalyst	η (@ 0.5 mA cm^{-2}) (mV)	η (@ 10 mA cm^{-2}) (mV)	A (mV/dec)	TOF @ η = 250 mV (μmol O_2 s^{-1} g^{-1})	TOF @ η = 300 mV (μmol O_2 s^{-1} g^{-1})
1	360	520	84.7 ± 2.1	0.23	0.89
2	300	470	73.3 ± 1.0	0.94	4.6
3	240	300	48.7 ± 0.7	7.1	78
4	230	290	47.5 ± 1.3	11	130
5	220	280	47.6 ± 0.6	21	220
6	220	350	42.0 ± 0.9 190 ± 11.6	19	42
7	210	270	45.2 ± 0.7 139 ± 35.6	33	290
8	200	260	44.7 ± 2.0 294 ± 90.6	53	290
Ni oxide	280	370	41.5 ± 0.6 170 ± 52.0	0.63	10

A comparison with published Fe–Ni-based water oxidation catalysts is provided in Table S3. Direct comparability of catalytic activity is in general problematic because of variations in mass loading, film thickness, intricate details of the electrochemical measurements, such as electrode substrate, rotation speed and dwell time to reach steady-state conditions or scan rates; also, overpotentials were recorded at different current densities. Nevertheless, we compiled published data and compared them with our catalysts made by PLAL. When measured at a current density of 10 mA cm^{-2} on a flat electrode substrate, our best catalyst had the lowest overpotential.

Table S3: Comparison of overpotentials η (at given current densities) of this work with reported catalysts. Electrode substrate materials are also given because only flat working electrode substrates allow for a meaningful comparison of electrocatalyst performance.

Catalyst	Electrode substrate	Current density (mA cm^{-2})	η (mV)	Reference
8	Flat HOPG	10	260	this work
5	Flat HOPG	10	280	this work
Thin-film solution-cast $Ni_{0.9}Fe_{0.1}O_x$	Au/Ti-coated quartz crystal	10	336	37
Nanostructured α-$Ni(OH)_2$	Glassy carbon	10	331	31
Electrodeposited $NiFeO_x$	Glassy carbon	10	360	38
Thin-film electrodeposited Ni-Fe (40% Fe)	Gold	10	280	27
Graphene FeNi double hydroxide hybrid	Ni foam, unspecified pore size*	10	220	39
Thin film nickel oxide with iron impurities	Nickel foil	8	230	23
Ni-Fe layered double hydroxide nanoplates	Carbon fiber paper	5	290	30

Catalyst	Electrode substrate	Current density (mA cm^{-2})	η (mV)	Reference
β-NiOOH	Nickel, polished with μm-sized alumina powders	5	500	40
Mixed Fe-Ni oxides	Carbon paper	1	375	41
Nickel-borate	Glassy carbon	1	425	1
Amorphous α-$Fe_{20}Ni_{80}O_x$	FTO glass	0.5	210	42
High surface-area nickel metal oxides	Nickel or steel microdiscs	0.5	265	43
$NiFeAlO_4$ inverse spinel	Glassy carbon	0.1	380	44
NiO_x deposited from molecular $[Ni(en)_3]^{2+}$	Glassy carbon	0.1	390	45

* The high porosity of nickel foam leads to an enlargement of the electrode substrate surface area relative to the apparent geometric area, inflating current densities that are normalized to the geometric electrode area.

References:

(1) Dincă, M.; Surendranath, Y.; Nocera, D. G. *Proc. Natl. Acad. Sci. U. S. A.* **2010**, *107*, 10337.
(2) Blakemore, J. D.; Gray, H. B.; Winkler, J. R.; Müller, A. M. *ACS Catal.* **2013**, *3*, 2497.
(3) Barr, T. L.; Seal, S. *J. Vac. Sci. Technol. A* **1995**, *13*, 1239.
(4) Shirley, D. A. *Phys. Rev. B* **1972**, *5*, 4709.
(5) Downs, R. T. The RRUFF Project: an integrated study of the chemistry, crystallography, Raman and infrared spectroscopy of minerals. Program and Abstracts of the 19th General Meeting of the International Mineralogical Association in Kobe, Japan. O03-13, 2006.
(6) Rasband, W. S.; ImageJ; U.S. National Institutes of Health: Bethesda, MD. Available online at http://imagej.nih.gov/ij/.
(7) Oelßner, W.; Berthold, F.; Guth, U. *Mater. Corros.* **2006**, *57*, 455.
(8) King, R. N.; ESCA Binding Energy Chart, Surface Science Instruments: Mountain View, CA.
(9) Temesghen, W.; Sherwood, P. *Anal. Bioanal. Chem.* **2002**, *373*, 601.
(10) X-ray Photoelectron Spectroscopy Database 20, Version 4.1 (National Institute of Standards and Technology, Gaithersburg, 2012); http://srdata.nist.gov/xps/.
(11) Biesinger, M. C.; Payne, B. P.; Lau, L. W. M.; Gerson, A.; Smart, R. S. C. *Surf. Interface Anal.* **2009**, *41*, 324.
(12) You, S. S.; Rashkov, R.; Kanjanaboos, P.; Calderon, I.; Meron, M.; Jaeger, H. M.; Lin, B. *Langmuir* **2013**, *29*, 11751.
(13) Powder diffraction file no. 01-076-6119 (ICDD, 2012).
(14) Powder diffraction file no. 00-038-0715 (ICDD, 2012).
(15) Shebanova, O. N.; Lazor, P. *J. Solid State Chem.* **2003**, *174*, 424.
(16) Mazzetti, L.; Thistlethwaite, P. J. *J. Raman Spectrosc.* **2002**, *33*, 104.
(17) Hall, D. S.; Lockwood, D. J.; Poirier, S.; Bock, C.; MacDougall, B. R. *J. Phys. Chem. A* **2012**, *116*, 6771.
(18) Bode, H.; Dehmelt, K.; Witte, J. *Electrochim. Acta* **1966**, *11*, 1079.
(19) McBreen, J. In *Handbook of Battery Materials*; Besenhard, J. O., Ed.; Wiley-VCH: Weinheim, 1999.
(20) Michael E. G Lyons, M. P. B. *Int. J. Electrochem. Sci.* **2008**, *3*, 1386.
(21) Lu, P. W. T.; Srinivasan, S. *J. Electrochem. Soc.* **1978**, *125*, 1416.
(22) Oliva, P.; Leonardi, J.; Laurent, J. F.; Delmas, C.; Braconnier, J. J.; Figlarz, M.; Fievet, F.; Guibert, A. d. *J. Power Sources* **1982**, *8*, 229.
(23) Corrigan, D. A. *J. Electrochem. Soc.* **1987**, *134*, 377.
(24) Bernard, M. C.; Bernard, P.; Keddam, M.; Senyarich, S.; Takenouti, H. *Electrochim. Acta* **1996**, *41*, 91.
(25) Kim, M. S.; Kim, K. B. *J. Electrochem. Soc.* **1998**, *145*, 507.
(26) Wehrens-Dijksma, M.; Notten, P. H. L. *Electrochim. Acta* **2006**, *51*, 3609.
(27) Louie, M. W.; Bell, A. T. *J. Am. Chem. Soc.* **2013**, *135*, 12329.
(28) Li, Y.-F.; Selloni, A. *ACS Catal.* **2014**, *4*, 1148.

(29) Bediako, D. K.; Lassalle-Kaiser, B.; Surendranath, Y.; Yano, J.; Yachandra, V. K.; Nocera, D. G. *J. Am. Chem. Soc.* **2012**, *134*, 6801.
(30) Gong, M.; Li, Y.; Wang, H.; Liang, Y.; Wu, J. Z.; Zhou, J.; Wang, J.; Regier, T.; Wei, F.; Dai, H. *J. Am. Chem. Soc.* **2013**, *135*, 8452.
(31) Gao, M.; Sheng, W.; Zhuang, Z.; Fang, Q.; Gu, S.; Jiang, J.; Yan, Y. *J. Am. Chem. Soc.* **2014**, *136*, 7077.
(32) Kermarec, M.; Carriat, J. Y.; Burattin, P.; Che, M.; Decarreau, A. *J. Phys. Chem.* **1994**, *98*, 12008.
(33) Hannoyer, B.; Ristić, M.; Popović, S.; Musić, S.; Petit, F.; Foulon, B.; Dalipi, S. *Mater. Chem. Phys.* **1998**, *55*, 215.
(34) White, W. B.; DeAngelis, B. A. *Spectrochim. Acta A* **1967**, *23*, 985.
(35) Musić, S.; Popović, S.; Dalipi, S. *J. Mater. Sci.* **1993**, *28*, 1793.
(36) Rajendran, S.; Rao, V. S. *J. Mater. Sci.* **1994**, *29*, 5673.
(37) Trotochaud, L.; Ranney, J. K.; Williams, K. N.; Boettcher, S. W. *J. Am. Chem. Soc.* **2012**, *134*, 17253.
(38) McCrory, C. C. L.; Jung, S.; Peters, J. C.; Jaramillo, T. F. *J. Am. Chem. Soc.* **2013**, *135*, 16977.
(39) Long, X.; Li, J.; Xiao, S.; Yan, K.; Wang, Z.; Chen, H.; Yang, S. *Angew. Chem., Int. Ed. Engl.* **2014**, *53*, 7584.
(40) Yeo, B. S.; Bell, A. T. *J. Phys. Chem. C* **2012**, *116*, 8394.
(41) Landon, J.; Demeter, E.; İnoğlu, N.; Keturakis, C.; Wachs, I. E.; Vasić, R.; Frenkel, A. I.; Kitchin, J. R. *ACS Catal.* **2012**, *2*, 1793.
(42) Smith, R. D. L.; Prévot, M. S.; Fagan, R. D.; Trudel, S.; Berlinguette, C. P. *J. Am. Chem. Soc.* **2013**, *135*, 11580.
(43) Li, X.; Walsh, F. C.; Pletcher, D. *Phys. Chem. Chem. Phys.* **2011**, *13*, 1162.
(44) Chen, J. Y. C.; Miller, J. T.; Gerken, J. B.; Stahl, S. S. *Energy Environ. Sci.* **2014**, *7*, 1382.
(45) Singh, A.; Chang, S. L. Y.; Hocking, R. K.; Bach, U.; Spiccia, L. *Energy Environ. Sci.* **2013**, *6*, 579.